An ALMA survey of the S2CLS UDS field: optically invisible submillimetre galaxies

Ian Smail [1]★ U. Dudzevičiūtė [1] S. M. Stach,[1] O. Almaini [2] J. E. Birkin [1] S. C. Chapman,[3] Chian-Chou Chen [4] J. E. Geach [5] B. Gullberg [6] J. A. Hodge,[7] S. Ikarashi,[1] R. J. Ivison [8] D. Scott,[9] Chris Simpson,[10] A. M. Swinbank [1] A. P. Thomson,[11] F. Walter,[12] J. L. Wardlow[13] and P. van der Werf[7]

[1]*Centre for Extragalactic Astronomy, Department of Physics, Durham University, South Road, Durham DH1 3LE, UK*
[2]*School of Physics and Astronomy, University of Nottingham, University Park, Nottingham NG7 2RD, UK*
[3]*Department of Physics and Atmospheric Science, Dalhousie University, Halifax, NS B3H 3J5, Canada*
[4]*Academia Sinica Institute of Astronomy and Astrophysics, No. 1, Section 4, Roosevelt Road, Taipei 10617, Taiwan*
[5]*Centre for Astrophysics Research, Department of Physics, Astronomy & Mathematics, University of Hertfordshire, Hatfield AL10 9AB, UK*
[6]*Onsala Space Observatory, Chalmers University of Technology, SE-439 92 Onsala/85748 Garching bei München, Sweden*
[7]*Leiden Observatory, Leiden University, PO Box 9513, NL-2300 RA Leiden, the Netherlands*
[8]*European Southern Observatory, Karl Schwarzschild Strasse 2, 85748 Garching bei München, Germany*
[9]*Department of Physics and Astronomy, University of British Columbia, 6224 Agricultural Road, Vancouver, BC V6T 1Z1, Canada*
[10]*Gemini Observatory Northern Operations Center, NSF's National Optical–Infrared Astronomy Research Laboratory, 650 North A'ohōkū Place, Hilo, HI 96720, USA*
[11]*Department of Physics and Astronomy, The University of Manchester, Oxford Road, Manchester M13 9PL, UK*
[12]*Max-Planck-Institut für Astronomie, Königstuhl 17, D-69117 Heidelberg, Germany*
[13]*Department of Physics, Lancaster University, Lancaster LA1 4YB, UK*

ABSTRACT

We analyse a robust sample of 30 near-infrared-faint ($K_{AB} > 25.3$, 5σ) submillimetre galaxies (SMGs) selected from a 0.96 deg^2 field to investigate their properties and the cause of their faintness in optical/near-infrared wavebands. Our analysis exploits precise identifications based on Atacama Large Millimeter Array (ALMA) 870-μm continuum imaging, combined with very deep near-infrared imaging from the UKIDSS Ultra Deep Survey. We estimate that SMGs with $K_{AB} > 25.3$ mag represent 15 ± 2 per cent of the total population brighter than $S_{870} = 3.6$ mJy, with a potential surface density of ∼450 deg^{-2} above $S_{870} \geq 1$ mJy. As such, they pose a source of contamination in surveys for both high-redshift 'quiescent' galaxies and very high redshift Lyman-break galaxies. We show that these K-faint SMGs represent the tail of the broader submillimetre population, with comparable dust and stellar masses to $K_{AB} \leq 25.3$ mag SMGs, but lying at significantly higher redshifts ($z = 3.44 \pm 0.06$ versus $z = 2.36 \pm 0.11$) and having higher dust attenuation ($A_V = 5.2 \pm 0.3$ versus $A_V = 2.9 \pm 0.1$). We investigate the origin of the strong dust attenuation and find indications that these K-faint galaxies have smaller dust continuum sizes than the $K_{AB} \leq 25.3$ mag galaxies, as measured by ALMA, which suggests their high attenuation is related to their compact sizes. We identify a correlation of dust attenuation with star formation rate surface density (Σ_{SFR}), with the K-faint SMGs representing the higher Σ_{SFR} and highest A_V galaxies. The concentrated, intense star formation activity in these systems is likely to be associated with the formation of spheroids in compact galaxies at high redshifts, but as a result of their high obscuration these galaxies are completely missed in ultraviolet, optical, and even near-infrared surveys.

Key words: galaxies: evolution – galaxies: formation – cosmology: observations – submillimetre: galaxies.

1 INTRODUCTION

Dust obscuration is a fundamental characteristic of ultraluminous infrared galaxies (ULIRGs, with far-infrared luminosities of $L_{IR} \geq 10^{12}$ L$_\odot$) at both low and high redshifts, with large columns of dust inferred as a necessary factor to explain the high infrared luminosities and their high ratios of far-infrared to optical emission (e.g. Houck et al. 1985; Harwit et al. 1987). High-redshift ULIRGs have typically

been found through single-dish sub/millimetre surveys at mJy-level brightnesses, and so are dubbed 'submillimetre' galaxies (SMGs), with lensed examples also frequently found in both far-infrared and longer wavelength studies (e.g. Negrello et al. 2010; Everett et al. 2020).

Observational evidence for optically faint (potentially highly dust-obscured or high-redshift) counterparts to SMGs has been presented since the earliest studies of this population (e.g. Rowan-Robinson et al. 1991; Dey et al. 1999; Smail et al. 1999; Dannerbauer et al. 2002, 2004; Dunlop et al. 2004; Frayer et al. 2004; Pope et al. 2005; Wang et al. 2007, 2011; Dannerbauer, Walter & Morrison 2008). Dey

★ E-mail: ian.smail@durham.ac.uk

et al. (1999) suggested that the very red optical–near-infrared colours of HR 10, a *K*-band-selected submillimetre-detected source at $z = 1.44$, are so extreme that if a similarly obscured galaxy existed at higher redshifts, $z \gtrsim 3$, it would be very challenging to detect in the optical or near-infrared, with $I_{AB} \gtrsim 31$ and $K_{AB} \gtrsim 27$ (see also Ivison et al. 2000; Weiss et al. 2009). Such an optically invisible, high-redshift SMG was detected in one of the earliest deep submillimetre maps in the Hubble Deep Field (HDF): labelled HDF 850.1 and subsequently identified using submillimetre interferometry (Cowie et al. 2009; Walter et al. 2012), corresponding to an SMG at $z = 5.18$ that is undetected in the very deep optical and near-infrared imaging available for this field ($I_{814} \geq 29$).

The early results hinted that high redshift and/or high dust attenuation can easily cause a distant ULIRG to be undetectable in even the deepest optical or near-infrared imaging. Such properties have implications for a range of studies. First, it means that care needs to be taken when using the presence of a near-infrared counterpart as an indication of the reality of a submillimetre detection (e.g. Aravena et al. 2016; Dunlop et al. 2017), or similarly when searching for potential optical/near-infrared counterparts in larger error circles than justified by the positional uncertainty. This is true even when using apparently very deep *Hubble Space Telescope* imaging given the telescope's surface brightness sensitivity and inability to operate longward of 1.6 µm. In addition, the extremely red colours of these systems mean that they represent a potential source of contamination in studies of high-redshift 'quiescent' or 'post-starburst' galaxies (e.g. Simpson et al. 2017; Schreiber et al. 2018) and also in surveys for high-redshift galaxies employing Lyman-break techniques (e.g. Mobasher et al. 2005; Pirzkal et al. 2013).

The most distant, highly obscured counterparts to submillimetre sources are particularly hard to identify without deep sub/millimetre interferometry (e.g. An et al. 2019). The advances made over the last decade in the sensitivity of observations in these bands, driven by the Atacama Large Millimeter Array (ALMA) and the upgrades to the Submillimeter Array and the Northern Extended Millimeter Array, have substantially increased the numbers of these systems available for study. Simpson et al. (2014) analysed ALMA 870-µm continuum observations of ∼100 single-dish submillimetre sources from Hodge et al. (2013) and found 19 SMGs that were undetected in one or more of the *Spitzer* IRAC bands between 3.6 and 8.0 µm (half of these SMGs either were undetected in *all* four IRAC bands or had at most a detection in a single band). They proposed that these near/mid-infrared-faint SMGs lie at somewhat higher redshift, and either have lower stellar masses or are more obscured than the bulk of the optical/near-infrared-detected population (Simpson et al. 2014, see also da Cunha et al. 2015). They also highlighted that at least one of these sources is an SMG at $z = 4.4$ whose redshift had been identified by Swinbank et al. (2012) through the serendipitous detection of the [C II] emission line in their ALMA observations. A subsequent analysis of the same sample by da Cunha et al. (2015), using the energy-balance spectral energy distribution (SED) modelling code MAGPHYS (da Cunha, Charlot & Elbaz 2008), suggested that the optical/near-infrared faintness of these sources is indeed due to a combination of redshift and dust obscuration.

The completion of interferometric mosaics covering 'blank fields' (rather than targeting known submillimetre sources detected in panoramic single-dish surveys, as done by Simpson et al. 2014) has also turned up a number of optical/near-infrared-faint SMGs. Franco et al. (2018) discussed four ALMA-detected sources in the GOODS-S region that lacked H_{160} detections, two of which are in the earlier Simpson et al. (2014) study (see also Zhou et al. 2020). Yamaguchi et al. (2019) found two examples in similar ALMA observations of

the same region (one previously identified by Cowie et al. 2018), while Umehata et al. (2020) obtained a spectroscopic redshift of $z = 3.99$ for a near-infrared-faint source uncovered in an ALMA survey in the SSA 22 region. There have also been examples studied through the selection of sources with very red *Herschel* SPIRE colours (e.g. Ikarashi et al. 2017), and simply through serendipitous sources discovered in ALMA observations (e.g. Williams et al. 2019). Finally, Wang et al. (2019), building on previous work that connected galaxies having extremely red near-infrared colours with submillimetre sources (e.g. Smail et al. 1999; Im et al. 2002; Coppin et al. 2004; Frayer et al. 2004), obtained ALMA snapshot continuum observations of a sample of 63 sources with very red $H_{160} - m_{4.5}$ colours and detected 39 of these with 870-µm flux densities, S_{870}, of $S_{870} \geq 0.6$ mJy.

To better understand the physical properties of optical/near-infrared-faint SMGs, we exploit a large ALMA SMG survey by Stach et al. (2019), who catalogued 708 SMGs from 870-µm interferometric continuum follow-up observations of 716 SCUBA-2 submillimetre sources in the SCUBA-2 Cosmology Legacy Survey (S2CLS; Geach et al. 2017) map of the UKIDSS Ultra Deep Survey (UDS; Lawrence et al. 2007; Almaini et al., in preparation). Dudzevičiūtė et al. (2020) presented an analysis of the multiwavelength properties of these ALMA-identified SMGs. Here, we focus on the subset of these SMGs that are faint or undetected in the very deep *K*-band imaging ($K_{AB} = 25.3$, 5σ) obtained for the UDS region by Almaini et al. (in preparation), and use this statistically robust sample to investigate the nature of these very faint and very red SMGs. We assume a cosmology with $\Omega_M = 0.3$, $\Omega_\Lambda = 0.7$, and $H_0 = 70 \, \text{km} \, \text{s}^{-1} \, \text{Mpc}^{-1}$; all quoted magnitudes are on the AB system and errors on median values are derived from bootstrap resampling. In this cosmology, at the median redshift of our $K_{AB} > 25.3$ mag SMG sample, $z = 3.4$, 1 arcsec corresponds to 7.5 kpc.

2 OBSERVATIONS AND ANALYSIS

Our analysis is based on the multiband photometric catalogue of 707 ALMA-located SMGs in the UKIDSS UDS field, constructed by Dudzevičiūtė et al. (2020) from the original ALMA catalogue in Stach et al. (2019). We provide a brief summary of the catalogue here and we refer the reader to those papers for the full details.

2.1 Sample selection

Stach et al. (2019) obtained ALMA Band 7 continuum observations in Cycles 1, 3, 4, and 5 of a complete sample of $716 > 4\sigma$ ($S_{850} \geq 3.6$ mJy) single-dish submillimetre sources selected from the 0.96-deg² S2CLS 850-µm map of the UDS field (Geach et al. 2017). Stach et al. (2019) catalogued 708 sources within the primary beam areas of these observations above a threshold of 4.3σ (corresponding to a false-positive rate of two per cent) based on maps tapered to a uniform resolution of 0.5-arcsec FWHM (full width at half-maximum). The 707 SMGs have fluxes of $S_{870} = 0.6$–13.6 mJy, after removing the brightest source, which corresponds to a strongly lensed SMG identified by Ikarashi et al. (2011).

Dudzevičiūtė et al. (2020) utilized the multiband imaging of the UDS field gathered by Almaini et al. (in preparation) to construct broad-band SEDs of the ALMA sources. This imaging includes the DR11 UKIRT WFCAM observations of the UDS in *JHK*, reaching 5σ depths of $J = 25.6$, $H = 25.1$, and $K = 25.3$, as well as deep *UBVRi'z'Y* imaging from Subaru, VISTA, and Canada–France–Hawaii Telescope. In addition, deep *Spitzer* IRAC/MIPS 3.6–24 µm coverage is provided by the SpUDS survey (PI: J. Dunlop; see

Caputi et al. [2011](https://academic.oup.com/mnras/article/502/3/3426/6127308)), 1.4-GHz radio observations come from UDS20 survey (Arumugam et al. in preparation; for a summary see Simpson et al. 2013), while *Herschel* SPIRE 250–500 μm photometry was deblended using the ALMA sources (as well as radio and MIPS priors) following Swinbank et al. (2014). Dudzevičiūtė et al. (2020) employed the MAGPHYS photo-*z* energy-balance modelling code (da Cunha et al. 2015; Battisti et al. 2019) to fit this multiband photometry. Derived parameters include photometric redshifts (z), far-infrared luminosities (8–1000 μm, L_{IR}), dust masses (M_d), and *V*-band attenuation (A_V), see Dudzevičiūtė et al. (2020) for more details of the models and the extensive tests that were applied using both observed and simulated data. We note that as we are studying a population whose SEDs include significant numbers of filters with no detections, we have tested the sensitivity of the photometric redshifts to changing the definitions of these limits. We vary the expected fluxes either to be 0 or 1.5σ in either the wavebands shortward of an observed wavelength of 8 μm (in the optical/near-infrared), or longward (in the far-infrared/submillimetre), or both. In this way, we confirm that the offsets are no larger than $\sim$0.05 in $\Delta z/(1 + z)$ with a scatter of $\sim$0.1–0.2 (see also Dudzevičiūtė et al. 2020).

To isolate a sample of $K > 25.3$ mag SMGs we first apply an 870-μm signal-to-noise (SNR) threshold (in a 0.5-arcsec aperture) of $\geq$4.8σ to our ALMA catalogue. This threshold corresponds to a false-positive rate of one source in the sample 637 SMGs with SNR $\geq$ 4.8 across the $\sim$50 arcmin^2 combined area mapped with ALMA, based on the detection rate of false sources in the inverted maps (Stach et al. 2019). We choose this more conservative threshold since we are studying the properties of the near-infrared-faint subset of the SMG population that would otherwise potentially suffer significant contamination from spurious ALMA sources if we allowed a higher false-positive rate. We then restrict the sample to those sources falling within the footprint of the very deep UKIDSS DR11 UDS *K*-band observations and having coverage in more than 10 broad-band filters in the optical/near-infrared, including observations in all four *Spitzer* IRAC channels. This provides an initial sample of 496 SMGs (271 of these have $S_{870} \geq 3.6$ mJy, the flux density limit of the parent SCUBA-2 survey of the UDS), of which 80 do not have a catalogued *K*-band counterpart brighter than the 5σ limit of the UDS *K*-band imaging: $K = 25.3$ mag in a 2-arcsec diameter aperture. We adopt this *K*-band limit as it is broadly representative of the detection limit for extended sources in current ground- and space-based near-infrared surveys (e.g. $H_{160} \sim 26$ in the CANDELS WFC3 imaging used by Franco et al. 2018).

We then visually check these sources in the DR11 *K*-band image (rebinned 2 × 2 to 0.26 arcsec pixel^{-1} sampling to increase the visibility of faint sources) to remove those with bright nearby galaxies within a 5-arcsec diameter region, which may contaminate the optical/near-infrared photometry (some of these may also be gravitationally lensing the SMG, although only by modest factors), or ambiguous cases where a faint *K*-band counterpart lies within 2 arcsec, where the offset between the submillimetre and near-infrared emission could plausibly be due to different levels of dust obscuration within a single galaxy. This gives a sample of 30 *K*-faint SMGs where we are confident that the 2-arcsec diameter photometry of the submillimetre sources is not contaminated by other nearby galaxies. We focus our analysis on this *K*-faint subset, while noting that they are expected to be broadly representative of the larger full sample of 80 $K > 25.3$ mag SMGs, but with more robust photometry. These 30 SMGs are AS2UDS IDs 0020.1, 0024.0, 0042.0, 0058.0, 0137.1, 0161.0, 0186.0, 0205.0, 0206.0, 0215.0, 0219.0, 0236.0, 0257.0, 0309.0, 0310.0, 0317.0, 0346.0, 0355.0, 0369.0, 0410.1, 0444.0, 0454.0, 0460.0, 0544.0, 0564.0, 0578.0, 0639.0, 0664.0, 0685.0, and

0690.0. Five of these fall in the CANDELS WFC3 coverage of the UDS and we have confirmed that none of these are detected above $H_{160} \sim 26.0$–26.3 (5σ).

In addition, we construct a control sample from the *K*-detected SMGs, selected to have the same photometric redshift distribution and L_{IR} as the *K*-faint sample, to allow comparisons free of the evolutionary (and selection) trends seen in the broader population (e.g. Stach et al. 2019; Dudzevičiūtė et al. 2020). We do this by searching around each of the SMGs in the *K*-faint sample for the nearest SMGs in the *K*-detected sample within $\Delta = 0.1$ in both z and $\log_{10} L_{IR}$. Removing duplicate matches, this leaves us with a sample of 100 *K*-detected SMGs in our *'control'* sample, that are matched in redshift and L_{IR} to the 30 *K*-faint SMGs.

2.2 Photometric properties

The median submillimetre flux density for the *K*-faint sample of 30 SMGs is $S_{870} = 3.8 \pm 0.3$ mJy (which is identical to the median of the whole sample of 496 SMGs). Eleven of these 30 SMGs are detected in the *Herschel* SPIRE or PACS bands, or at 1.4 GHz with the VLA (see Dudzevičiūtė et al. 2020), a marginally lower rate than the 60 per cent seen in the *control*, both rates reflecting their typically modest submillimetre brightness and the high redshifts of the sources. Of the three radio-detected *K*-faint SMGs, the most noteworthy is AS2UDS 0454.0, which is a radio-loud AGN with $S_{1.4} = 0.6$ mJy at $z = 3.5^{+0.8}_{-0.7}$ (see Algera et al. 2020).

Fig. 1 shows false-colour images of SMGs from our sample using the *J*, *K*, and $3.6 + 4.5$ μm passbands. By selection all of the galaxies are both very faint in the near/mid-infrared and if detected they display very red colours. When detected in the IRAC bands, the galaxies are typically compact in this $\sim$2-arcsec FWHM imaging. Since we are studying *K*-faint SMGs, these are neither detected individually in the higher resolution *K*-band imaging nor in a *K*-band stack (see below), with sufficient SNR to measure a reliable size, although the stacked source sizes are not inconsistent with the $R_e = 4.4^{+1.1}_{-0.5}$ kpc reported in the H_{160} band by Chen et al. (2015) for *H*-band-detected SMGs at $z = 1$–3.

To place limits on the characteristic near-infrared brightness of these systems we stack the sample of 30 SMGs in the UDS *J*- and *K*-band imaging (Almaini et al. in prep.) and obtain a marginal detection in the *K* band, with an average magnitude of $K = 26.0 \pm 0.5$, with the sources undetected in the *J* band, corresponding to a 3σ limit of $J \gtrsim 27.5$. Of the 30 SMGs in the *K*-faint sample, 16 are detected in one or more of the *Spitzer* IRAC channels at 3.6–8.0 μm, with the median magnitudes of these detected sources being $m_{3.6} = 23.3 \pm 0.2$, $m_{4.5} = 22.9 \pm 0.3$, $m_{5.8} = 22.1 \pm 0.1$, and $m_{8.0} = 22.1 \pm 0.1$. We stack the IRAC imaging of the remaining 14 undetected SMGs and obtain a weak detection at 4.5 μm and limits in the other bands: $m_{4.5} = 24.7 \pm 0.3$, $m_{3.6} \geq 24.9$, $m_{5.8} \geq 23.5$, and $m_{8.0} \geq 23.5$ (3σ limits). The IRAC 4.5-μm band is the reddest deep band and so it is unsurprising that we detect the sources in this filter and not in the bluer 3.6-μm channel or the shallower 5.8- or 8.0-μm channels. The 14 *K*-faint SMGs that lack individual IRAC detections are the most challenging sources to study, owing to the absence of constraints on their broad-band SEDs. Nevertheless, we note that of the 14, five are detected in SPIRE, PACS, or radio bands, leaving only nine with no additional constraints on their SEDs other than limits. We stress that our adoption of a $\geq$4.8σ ALMA selection means that at most one of these sources is expected to be spurious. The median ALMA flux density of these nine SMGs is consistent with the full sample, $S_{870} = 3.6 \pm 0.6$ mJy, and in addition two of them are independently detected by Ikarashi et al. (2015). One of
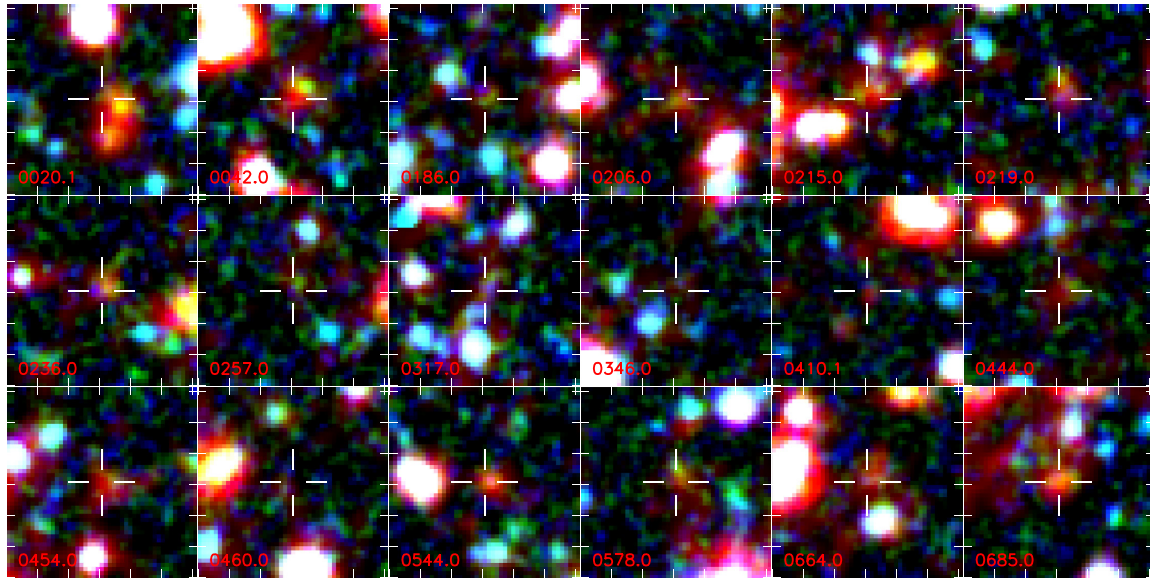
Figure 1. False-colour images (*J*, *K*, and 3.6 + 4.5 μm as the blue, green, and red channels, respectively) centred on SMGs from our *K*-faint sample, with the cross-hair marking the position of the ALMA source in each field. The typically very red near-infrared colours of these galaxies, as well as their faintness, are clear. Each panel is 12 arcsec square and the *J*- and *K*-band images have been smoothed with 0.5-arcsec FWHM Gaussians to enhance the visibility of faint emission.

these, AS2UDS 0186.0 is one of the two SMGs with very faint near-infrared counterparts and compact dust continuum emission studied by Ikarashi et al. (2017), ASXDF1100.053.1, who suggested the very red far-infrared/submillimetre colours of these galaxies indicated that they lay at high redshifts, $z \gtrsim 4$.

2.3 Structural properties

In addition to the parameters derived from the SED modelling, our analysis also exploits dust continuum sizes for a subset of the AS2UDS sample from Gullberg et al. (2019). This size information is available because a large fraction of the multicycle ALMA observations taken for the Stach et al. (2019) survey were obtained with the array in moderately extended configurations, yielding synthesized beams with angular sizes of ~0.2 arcsec, sufficient to reliably resolve the dust emission in those sources detected at sufficient SNR (SNR $\geq$ 8). Gullberg et al. (2019) present circularized effective radii, R_e, for 153 SMGs detected at SNR $\geq$ 8, from fitting Sersic $n = 1$ profiles to the 870-μm continuum images.[1]

We highlight two critical facts about these observations: first, while the sources are well fitted by exponential surface brightness profiles, the ellipticity distribution of the sources suggests that the dust continuum emission arises not from a disc, but from tri-axial structures, most likely bars (see Gullberg et al. 2019). This supports the conclusions from deeper, high-resolution imaging of a smaller sample of SMGs by Hodge et al. (2016, 2019) that directly resolves bar-like structures in those sources. The second issue to note is that the shallow AS2UDS observations only detect the highest surface brightness components, with Gullberg et al. (2019) showing from a stacking analysis that in addition to these high surface brightness, compact components (with $R_e \sim 0.1$ arcsec, or ~1 kpc), a typical

source also has a fainter, more extended exponential component ($R_e \sim 0.5$ arcsec, or ~4 kpc) that is undetected in the individual maps. This extended component has a size comparable to the stellar and gas discs in these systems (Gullberg et al. 2019; see also Calistro Rivera et al. 2019). To account for the contribution of this faint, extended component to the sizes we statistically correct the sizes using the flux-weighted sum of the measured R_e in Gullberg et al. (2019) and a 0.5-mJy component with $R_e \sim 0.5$ arcsec, as indicated by their stacking analysis. This accounts for the poor sensitivity of the high-resolution ALMA snapshot observations to the faint, extended emission in these sources. The *corrected* radius is then $R_e^{corr} = (S_{870} - 0.5)/S_{870} \times R_e^{true} + 0.5/S_{870} \times 0.5$ arcsec. The correction is a median of factor of $1.30^{+0.25}_{-0.13}$, where the error is the 16–84th percentile range, but we stress that this correction, while reproducing the average true sizes, will not recover the full dispersion of the true sizes.

In our analysis, we also include 870-μm sizes for nine *K*-bright SMGs that were also observed by Tadaki et al. (2020) in their deeper, high-resolution ALMA survey of a *K*-band-selected galaxies including the UDS field. A further two SMGs from Gullberg et al. (2019) have sizes reported by Tadaki et al. (2020) and these agree with the corrected values used here. We also employ the 42 remaining fainter UDS galaxies from Tadaki et al. (2020) with submillimetre detections at SNR $\geq$ 10 and measured sizes as a comparison sample in our work. To do this we use MAGPHYS to model their multiwavelength photometry, including the reported S_{870} fluxes, in an identical manner to that used for the AS2UDS sample by Dudzevičiūtė et al. (2020).

3 RESULTS AND DISCUSSION

We start by assessing the rate of *K*-faint SMGs in the overall SMG population. We adopt an ALMA flux density limit of $S_{870} \geq 3.6$ mJy to ensure that the sample is complete over the UDS field (see Stach et al. 2019), finding a lower limit of 17 SMGs from a parent population of 271 SMGs using our *K*-faint sample ($\geq 6 \pm 2$ per cent) and 42 examples (15 ± 2 per cent) from the full *K* > 25.3 sample, which are

[1]We caution that the values reported for the circularized $n = 1$ effective radii in table A1 in Gullberg et al. (2019), R_e^{A1}, are in error and actually list the minor-axis size; the true $n = 1$ circularized R_e can be easily recovered using the axial ratio (*b/a*) values in the table: $R_e = \sqrt{(R_e^{A1})^2/(b/a)}$.
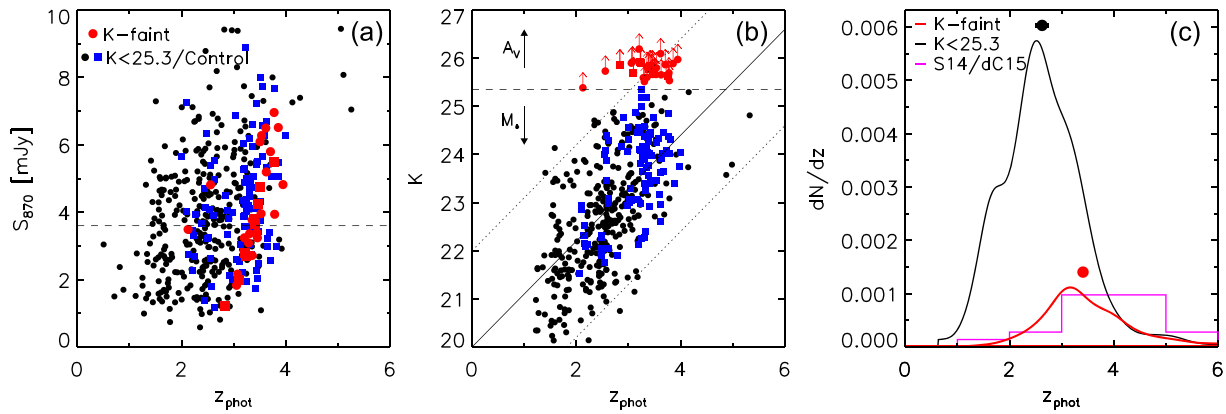
Figure 2. (a) Submillimetre flux density (S_{870}) versus median photometric redshift for the K-faint $K > 25.3$ mag sample, compared to the $K \leq 25.3$ mag SMGs in AS2UDS, where we highlight the sources in the z/L_{IR}-matched *control* sample. The K-faint sources have photometric redshifts that suggest they lie at higher redshifts than the majority of the K-detected SMGs. Although even at $z \gtrsim 3$–4 there is a mix, with the K-faint sample comprising at most $\sim$25–30 per cent of the SMG population. We identify the nine K-faint SMGs whose SEDs are constrained solely by photometric limits by plotting those as squares. The dashed line indicates the flux limit of the parent SCUBA-2 survey of the UDS field. (b) K-band magnitude versus photometric redshift for the $K \leq 25.3$ mag SMGs in AS2UDS and the K-faint sample (shown as a scatter of points fainter than the 5σ detection limit of $K = 25.3$, shown by the dashed line). The vectors indicate the influence of increasing stellar mass ($M_\star$) or attenuation (A_V). We show a linear fit to the median trend line as a solid line and the dotted lines offset by ± 2 mag that roughly delimit the boundaries of the distribution. Given the trends seen in the population, we conclude that the K-band magnitudes of the K-faint SMGs are consistent with being both higher redshift, but also either less massive or more dust attenuated. (c) The redshift distribution and median redshifts for the K-faint SMG sample compared to the K-detected AS2UDS SMGs and the distribution of near-infrared-faint SMGs from Simpson et al. (2014). The distributions for the AS2UDS samples are the average MAGPHYS PDFs from Dudzevičiūtė et al. (2020), while we show the binned MAGPHYS photometric redshifts from da Cunha et al. (2015) for the Simpson et al. (2014) sources (S14/dC15). We confirm the behaviour seen in panel (a) that the K-faint SMGs have a significantly higher median redshift than the K-detected sample: $z = 3.44 \pm 0.06$ (consistent with $z = 3.8 \pm 0.4$ for the Simpson et al. 2014 examples) and $z = 2.36 \pm 0.11$, respectively (close to the values reported for similar selections by Dudzevičiūtė et al. 2020). These estimates are based on the median of the individual redshifts for each distribution and we plot these and indicate their bootstrap uncertainty in the figure. The K-faint distributions have been normalized to reflect the number densities of their parent samples.

consistent with the 17 ± 1 per cent reported by Dudzevičiūtė et al. (2020). We therefore conclude that 15 ± 2 per cent of SMGs brighter than $S_{870} \geq 3.6$ mJy are near-infrared faint ($K \gtrsim 25.3$ mag). We see no significant variation in the fraction of K-faint SMGs with 870-μm flux density across the range $S_{870} = 3$–10 mJy.

Our measured K-faint SMG fraction is consistent with previous estimates of the fraction of K-faint sources in the SMG population based on smaller samples: 20 ± 4 per cent using the 19 sources in the Simpson et al. (2014) sample fainter than $K \sim 24.4$ (3σ); $\sim$20 per cent by Franco et al. (2018) based on four examples fainter than $H_{160} \sim 26$ (5σ, assuming a more realistic 1-arcsec source size rather than a point-source estimate – comparable to our $K = 25.3$ limit); and $\sim$8–20 per cent based on two firm candidates and three tentative sources fainter than $K = 24.8$ (5σ) from a parent sample of 25 SMGs in Yamaguchi et al. (2019). We note that all three of these estimates are for sources in the same field: Franco et al. (2018) have sources in common with Simpson et al. (2014), although the candidate lists for Yamaguchi et al. (2019) and Franco et al. (2018) do not overlap. Assuming that the fraction of K-faint SMGs does not change strongly with submillimetre flux density, which appears to be consistent with the trends in our sample, we derive a surface density of $K > 25.3$ mag and $S_{870} \geq 1$ mJy SMGs of 450^{+750}_{-300} deg^{-2}.

Wang et al. (2019) also estimate a surface density of ALMA-detected Extremely Red Objects (EROs, $H_{160} - m_{4.5} \geq 2.5$) of $\sim$530 deg^{-2} at $m_{4.5} \leq 24$, which is in reasonable agreement with our submillimetre-selected sample. This significant surface density of very red, optically/near-infrared-faint sources is an obvious concern for searches that rely on similar photometric selection to identify rare examples of high-redshift 'quiescent' or 'post-starburst' galaxies (e.g. Schreiber et al. 2018), as well as for very high redshift Lyman-

break galaxies (e.g. Pirzkal et al. 2013), especially if these do not allow for very high dust attenuations in the models of foreground contaminating populations.

One of the other basic characteristics of SMGs is the fraction of companions, termed 'multiplicity' (e.g. Ivison et al. 2007; Karim et al. 2013; Stach et al. 2018), which arises from a combination of physical associations and random projections (exacerbated by the blending in low-resolution single-dish submillimetre surveys, Simpson et al. 2020). For the K-faint sample of SMGs, we find three examples (0020.1, 0137.1, and 0410.1), all fainter than $S_{870} \sim 2$ mJy, which are secondary components in the fields of other SMGs and another three K-faint SMGs (0058.0, 0460.0, and 0564.0) are in fields with second fainter SMG. This rate of multiples is 20 per cent and is identical to the rate in the full sample (97/496, comprising three triples and 44 pairs). Four of the six K-faint SMGs have photometric redshift ranges that overlap with the neighbour SMG in their ALMA map (0020.1, 0137.1, 0410.1, and 0546.0). A simple simulation suggests that such an occurrence will happen in $\sim$10 per cent of cases by chance, so it is possible that these obscured sources are companions of less obscured SMGs at the same redshift, illustrating the potential diversity of the population, even at the same redshift (see Fig. 2).

Now we turn to the properties of the K-faint SMGs provided by the MAGPHYS analysis of Dudzevičiūtė et al. (2020). In Figs 2(a) and (b), we show the distributions of submillimetre flux density and K-band magnitude versus photometric redshift from MAGPHYS for the K-faint SMGs and the remainder of the SMG population with $K \leq 25.3$. These figures show that the K-faint subset lie at higher redshifts, but that not all high-redshift SMGs are K-faint: the proportion of K-faint SMGs at $z \geq 3$ is 28 ± 4 per cent of the population, so marginally

higher than the fraction for the total population. This suggests that another physical property contributes to the faintness of these sources in the *K*-band, not just their redshifts. The vectors plotted in Fig. 2(b) indicate the effect of increasing the stellar mass or dust attenuation in the sources, suggesting that *K*-faint SMGs either could be the lower mass or higher attenuation tail of the higher-than-average-redshift SMG population.

One weakness of the presentation of the samples in Figs 2(a) and (b) is the significant uncertainties in the photometric redshifts, particularly for those sources that are faint in the optical/near-infrared wavebands. For that reason, we also show in Fig. 2(c) the average redshift probability density functions (PDFs) from the MAGPHYS analysis of the *K*-faint SMGs, compared to the $K < 25.3$ mag subset and also the distribution for the equivalent *K*-faint SMGs from Simpson et al. (2014), using the MAGPHYS modelling results from da Cunha et al. (2015). These distributions confirm that the *K*-faint subset has a significantly higher median redshift compared to the *K*-detected sample: $z = 3.44 \pm 0.06$ versus $z = 2.36 \pm 0.11$. These values are comparable to those reported for similar selections by Dudzevičiūtė et al. (2020). Equally, the median redshift we derive for our *K*-faint sample is consistent with the $z = 3.8 \pm 0.4$ derived for the Simpson et al. (2014) examples by da Cunha et al. (2015). However, the median redshift is significantly below that claimed for this population by Franco et al. (2018), $z > 4$, and also the median redshift proposed for the ALMA-detected EROs in Wang et al. (2019), $z = 4.0 \pm 0.2$, but is consistent with the broad range suggested by Yamaguchi et al. (2019), $z \sim 3$–5.

We note that the expected difference in *K*-band brightness for an SMG at $z = 3.4$ compared to $z = 2.4$, based on the composite SMG SED from Dudzevičiūtė et al. (2020) is $\Delta K \sim 1.1$ mag. This difference in typical *K*-band magnitude is consistent with the median trend shown in Fig. 2(b), as well as the median *K* magnitudes of our redshift-matched *control* sample, $K = 23.9 \pm 0.1$ mag, compared to the full *K*-detected population, with $K = 22.8 \pm 0.1$ mag. We conclude that at least part of the explanation for the properties of *K*-faint SMGs arises from their higher redshifts, compared to the *K*-detected SMG population. However, as indicated by the two vectors in Fig. 2(b), it is not clear what other factors may be influencing the *K*-brightness of these SMGs.

The other key parameter that has been historically identified as a driver of extreme red optical/near-infrared colours in star-forming galaxies is dust attenuation, usually parametrized by *V*-band attenuation: A_V. We highlight that the rest-frame *V*-band corresponds roughly to observed *K* band for SMGs at $z \sim 3.5$, such as the *K*-faint population. Using the MAGPHYS analysis presented in Dudzevičiūtė et al. (2020), we derive a median *V*-band attenuation for the *K*-faint SMGs of $A_V = 5.2 \pm 0.3$, compared to $A_V = 2.9 \pm 0.1$ for the *control* sample, indicating that attenuation, as well as typically higher redshifts, are responsible for the faint near-infrared fluxes of the *K*-faint SMGs – as suggested by Dudzevičiūtė et al. (2020). We assess the variation in *K*-band flux for the *K*-faint and *K*-detected SMG samples versus z and A_V using maximal information-based non-parametric exploration (MINE; Reshef et al. 2011). This analysis suggests that both factors have an influence on the near-infrared fluxes of the *K*-faint SMGs that are an order of magnitude fainter than the typical *K*-detected SMG in our survey. Roughly half of this difference is a consequence of the typically higher redshift of the *K*-faint SMGs (as suggested by Simpson et al. 2014, see also da Cunha et al. 2015), with the remainder arising from their higher dust attenuation.

While the role of redshift in defining the *K*-faint SMG population is easy to understand (through the distance modulus and *K*-corrections)

what is the physical origin of the high dust attenuation seen in these systems, compared to the less extincted, *K*-detected SMGs at similar redshifts seen in Fig. 2? We show in Figs 3(a) and (b), the distributions of A_V for the *K*-faint SMG sample, compared to both the whole population and the *control* sample, as a function of two potential physical drivers: stellar mass (M_*, following Garn & Best 2010); and dust mass (M_d). We caution that the covariance in the parameters in the MAGPHYS models means that some care needs to be taken when trying to assess the physical significance of any apparent correlations. For example, the covariant errors between attenuation and inferred stellar age will mean that sources will move diagonally on the A_V–M_* plane. Nevertheless, we find no obvious trends, with the median stellar masses of the *K*-faint and *control* samples being consistent (although with the *control* showing a broader range), $10^{11.10 \pm 0.04}$ and $10^{11.00 \pm 0.06}$ M$_\odot$, as are the median dust masses, $10^{8.86 \pm 0.06}$ and $10^{8.98 \pm 0.04}$ M$_\odot$. This suggests that neither dust mass nor stellar mass are the drivers of the high dust attenuation of the *K*-faint SMGs.

As a brief aside, we note that Lagos et al. (2020) use their SHARK semi-analytical model to provide predictions for model SMGs with $S_{870} > 1$ mJy and $m_{3.6} > 23.5$ that roughly match the AS2UDS *K*-faint sample discussed here (see Section 2.2). The predicted properties of these sources in the model are a median redshift of $z = 3.5^{+0.9}_{-0.7}$, stellar mass of $10^{10.0 \pm 0.3}$ M$_\odot$, dust mass of $10^{7.5 \pm 0.6}$ M$_\odot$, and attenuation of $A_V = 2.2 \pm 0.5$. In comparison to the observational results above, the predicted median redshift from SHARK is in good agreement with that for our sample, while the stellar and dust masses appear to be an order of magnitude or more too low and the attenuation is ~ 3 mag too low. Hence, the model galaxies tend to be less obscured (indeed, less obscured than the *control* sample), but also much less massive and dust rich than the observed population.

Returning to the empirical correlations: to investigate how the size of the dust-emitting region might affect the optical/near-infrared properties of SMGs, we show in Fig. 3(c) the relation between A_V and R_e^{corr}. This suggests a moderate correlation with $A_V = (3.2 \pm 0.2) - (3.0 \pm 0.9) \times (R_e^{\mathrm{corr}} - \langle R_e \rangle)$ with an average $\langle R_e \rangle = 1.13$ kpc for the 33 sources in the combined *control* and *K*-faint SMG sample with measured sizes. To test the influence of the broader range in stellar mass seen in our *control* sample, compared to the *K*-faint SMGs (see Fig. 3a), on the trend in Fig. 3(c), we also restrict the *control* sample to the same stellar mass range seen for our *K*-faint SMGs, $M_\star = 10^{10.7}$–$10^{11.5}$ M$_\odot$, which reduces the sample to 69 sources. We then refit the trend, finding little change, with the gradient reducing to -2.8, and show this fit as the dashed line in Fig. 3(c).

The most striking feature of Fig. 3(c) is that the *K*-faint SMGs fall at the high A_V and small R_e end of the distributions. The median dust continuum size of the seven *K*-faint and 26 *control* SMGs with sizes are 1.00 ± 0.05 and 1.17 ± 0.04 kpc, with a Kolmogorov–Smirnov test indicating a three per cent chance of the two subsets being drawn from the same parent population. This suggests that it is the smaller dust continuum sizes that are connected to the high A_V, which in turn is responsible for the *K*-faint SMGs having the faintest rest-frame optical emission of SMGs at their redshifts. If correct, then the more compact dust emission in the *K*-faint SMGs ought to result in higher characteristic dust temperatures, given the two samples have near identical dust masses (cf. Scoville 2013). Indeed, this difference in sizes is reflected in a similar difference between the characteristic dust temperatures (assuming the same dust opacity) of the *K*-faint and *control* samples (for those SMGs with SPIRE detections): $T_d = 33.6 \pm 1.2$ K and $T_d = 30.9 \pm 1.0$ K, respectively, although this is not statistically significant, amounting to only a 1.7σ difference (see also da Cunha et al. 2015).
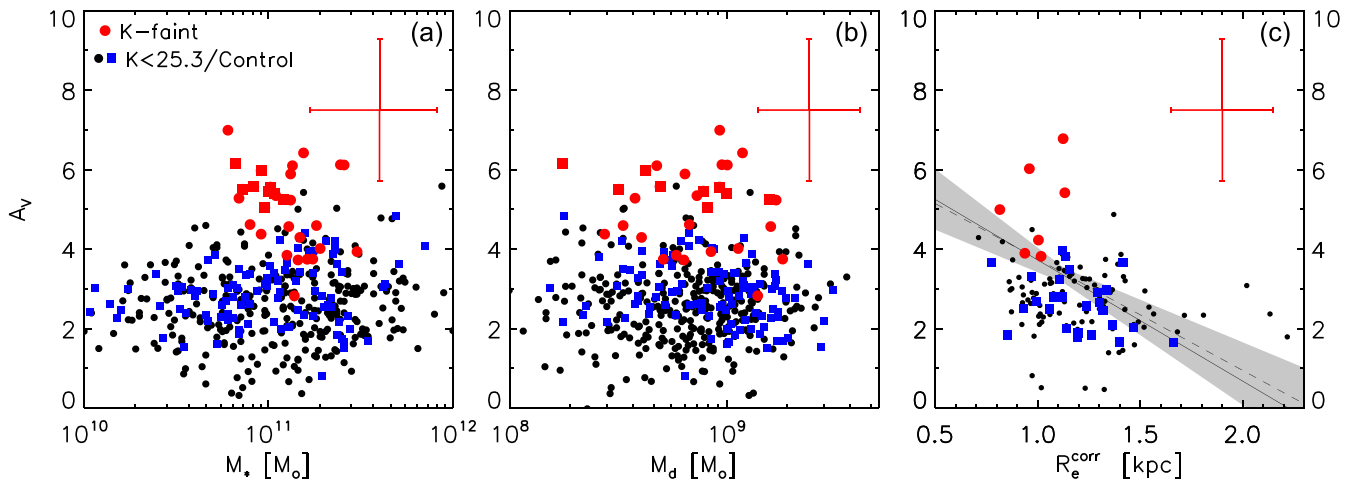
Figure 3. (a) Variation of V-band attenuation (A_V) with stellar mass (M_*) for the K-faint SMGs, compared to the population of K-detected SMGs with $K \leq 25.3$ mag. We see that the K-faint SMGs have higher A_V, as expected, but span only a modest range in stellar mass compared to the broader population (or the *control*), with typically high stellar masses of $M_* = 10^{11.10 \pm 0.04}$ M$_\odot$. We highlight the sources in the z/L_{IR}-matched *control* sample of the K-detected SMG population and we similarly identify the nine K-faint SMGs whose SEDs are constrained solely by photometric limits by plotting those as squares. (b) Variation of A_V with dust mass (M_d) for the K-faint SMGs compared to the sample of K-detected SMGs. Here, we see that the K-faint SMGs exhibit a broad range in M_d, comparable to that of the K-detected and *control* samples. (c) Variation of A_V with dust continuum size (R_e) for the subset of SMGs that have measurements from Gullberg et al. (2019). This shows a correlation for the combined *control* and K-faint samples, with the K-faint SMGs typically having smaller-than-average R_e, as well as higher-than-average A_V. We overplot a linear fit to the trend seen in the combined sample as a solid line and illustrate the 1σ uncertainties in this by the shaded region. To investigate the influence of stellar mass on this trend, we also restrict the *control* sample to the same stellar mass range seen for our K-faint SMGs, $M_\star = 10^{10.7} - 10^{11.5}$ M$_\odot$, and refit the trend, which is plotted as a dashed line, showing little change. In each panel, we illustrate the median fractional uncertainty in the parameters for the sources in the K-faint sample, based on the 16–84th percentile range of the relevant PDF from the MAGPHYS analysis (see Dudzevičiūtė et al. 2020).

To investigate the origin of the trend seen in Fig. 3(c), we show two plots in Fig. 4 that combine dust continuum sizes, dust attenuation and far-infrared luminosities. Fig. 4(a) illustrates the distribution of dust continuum size with far-infrared luminosity, while in Fig. 4(b) we combine these two parameters to yield the far-infrared surface brightness (as a proxy for star formation rate surface density, Σ_{SFR}), and plot this against dust attenuation. We caution that this assumes that the rest-frame ~ 200-μm dust continuum size reflects the extent of the far-infrared emission in these systems.

We show in Fig. 4(b) both our SMG sample and, to extend the dynamic range of the plots to search for correlations, also the typically fainter dust continuum-detected sources from Tadaki et al. (2020). We fit log-linear relations to the full distribution of sources in both these plots and derive median trends of $R_e = (1.45 \pm 0.14) - (0.53 \pm 0.31) \times \log_{10}(L_{IR}/\langle L_{IR} \rangle)$, where $\langle L_{IR} \rangle = 3.3 \times 10^{12}$ L$_\odot$, for Fig. 4(a) and $A_V = (2.72 \pm 0.09) + (0.82 \pm 0.13) \times \log_{10}(\Sigma_{IR}/\langle \Sigma_{IR} \rangle)$, with $\langle \Sigma_{IR} \rangle = 3.3 \times 10^{11}$ L$_\odot$ kpc^{-2}, in Fig. 4(b).

We note that the trends in Fig. 4 could be influenced by the difference in the median redshift of K-faint SMGs and the Tadaki et al. (2020) sample, which are $z \sim 3.4$ and $z \sim 2.2$, respectively. Studies of the stellar continuum sizes of star-forming galaxies suggest that these decline at higher redshift (e.g. van der Wel et al. 2014), and we illustrate in Fig. 4 how correcting for this effect could influence the median R_e and Σ_{IR}, based on an extrapolation of trend seen in similarly massive star-forming galaxies from van der Wel et al. (2014), assuming this evolution is reflected in their dust continuum sizes. We correct the Tadaki et al. sample to yield sizes expected for such sources at $z \sim 3.4$ and refit the trends, showing the resulting best-fitting lines in Figs 4(a) and (b).

We see that the observed trend of R_e–L_{IR} in Fig. 4(a) is weak and only marginally significant and becomes even weaker when we account for potential evolution of galaxy size with redshift.

Indeed, the behaviour might be better described as an increase in the range of R_e of the population at lower luminosities, although we caution that the statistical correction applied to the AS2UDS sample will not capture the variety of sizes in that sample. In contrast, the trend we see between A_V and Σ_{IR} is significant ($>6\sigma$) and does not appear to be driven by the Tadaki et al. (2020) sample, indicating that the MAGPHYS-derived dust attenuation does increase with far-infrared surface brightness (and less strongly with far-infrared luminosity). The K-faint SMGs have above-average Σ_{IR} for the AS2UDS sample, which given the measured correlation would lead to higher attenuation. However, we also find that the K-faint SMGs are indistinguishable in Σ_{IR} (or Σ_{SFR}) from the *control* sample, and they lie off the trend in terms of A_V, indicating that it is not solely their high surface brightnesses that are responsible for their high attenuation.

We also study the trends of dust attenuation with near-infrared size or the ratio of near-infrared/submillimetre size in the K-bright AS2UDS SMGs (and the sources from Tadaki et al. 2020). However, there are no clear trends that would explain the properties of the high A_V inferred for the K-faint SMGs, which obviously lack detectable near-infrared counterparts and hence sizes. Thus, we cannot conclusively explain the physical origin of the very high dust attenuation seen in this subset of the SMG population. Nevertheless, there are hints that this behaviour may result either from the relative scale of the obscured and less obscured components in these systems or other aspects of their geometry. Hodge et al. (2016) and Gullberg et al. (2019) have used high-resolution ALMA maps to demonstrate that the dust continuum emission of SMGs is generally well described by a Sersic $n = 1$ exponential, but the bulk of this emission does not arise from a smooth disc – instead, it traces compact bar-like structures (see Hodge et al. 2019), which likely represent dense gas structures driven by external gravitational torques or secularly
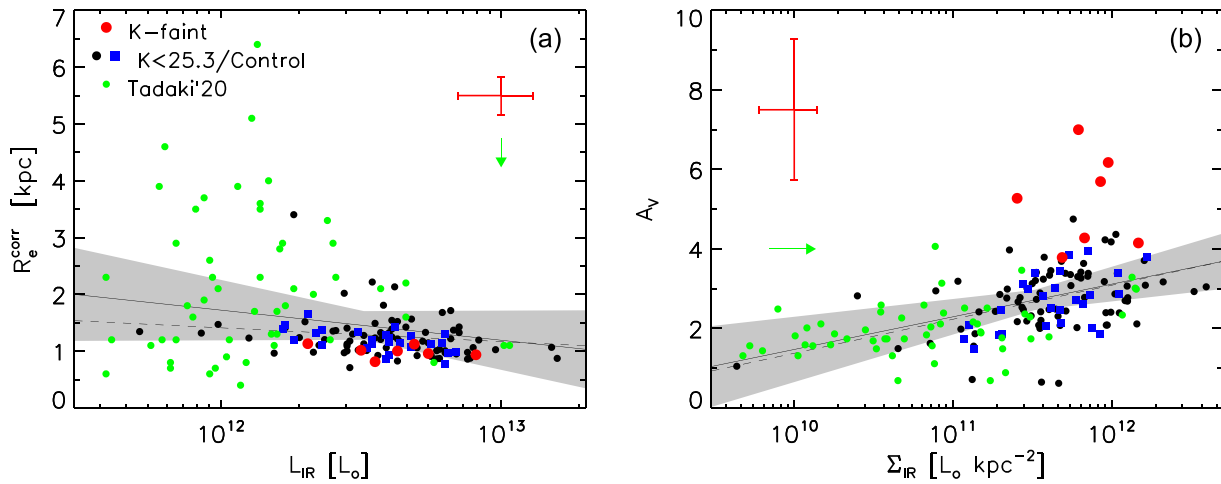
Figure 4. (a) Variation of the dust continuum size, R_e^{corr}, with far-infrared luminosity, L_{IR}, for the SMGs from Gullberg et al. (2019). R_e^{corr} are the effective radii that have been statistically corrected for the faint, extended component found in stacks of the population as described in Section 2. We identify the *K*-faint SMGs and those in our *control* sample and we also plot the typically fainter 870-μm-detected *K*-band-selected galaxies from Tadaki et al. (2020). We find a weak trend of increasing size at fainter luminosities (or simply a wider range in sizes), but with considerable scatter. We fit a linear relation to the combined sample and show this as a solid line and the 1σ uncertainty as the shaded region. The median uncertainties for the *K*-faint SMGs are illustrated by the error bars and we also show the vector corresponding to the expected shift in the median size of the Tadaki et al. (2020) from the difference in median redshift, compared to the *K*-faint SMGs, assuming the evolution for massive, star-forming galaxies presented in van der Wel et al. (2014). The dashed line shows the best-fitting trend including this correction, which is even weaker. (b) Variation of the *V*-band attenuation, A_V, with far-infrared surface brightness, Σ_{IR}, for the SMGs from Gullberg et al. (2019) and the *K*-band-selected sources from Tadaki et al. (2020). We identify a correlation between dust attenuation and far-infrared surface brightness (which is a proxy for star formation rate surface density: Σ_{SFR}), with the *K*-faint SMGs appearing as outliers to the trend. We fit a linear relation to the combined sample and show this as a solid line and the 1σ uncertainty as the shaded region. The vector indicates the shift in the median Σ_{IR} for the Tadaki et al. (2020) sample if we adopt the redshift–size evolution from van der Wel et al. (2014) and the dashed line shows the negligible change that results in the best fit. We use the same symbol as in the left-hand panel and again the median uncertainties for the *K*-faint SMGs are illustrated by the error bars.

generated internal structures in these gas-rich galaxies [similarly, the faint spatially extended exponential halo found by Gullberg et al. (2019) in their stacks may represent dust emission from the stellar/gas disc]. Thus, the smaller sizes we infer for the *K*-faint SMGs suggest that they may host concentrated dust-obscured activity (perhaps lacking a larger disc component), which is at least in part responsible for the inferred high attenuations. However, the absence of detectable rest-frame optical emission in these systems also suggests that they lack a spatially extended and less obscured stellar component (as seen in the optically brighter and lower redshift subset of SMGs; e.g. Chen et al. 2015).

The absence of an extended, less obscured stellar component may be an increasingly frequent feature of SMGs at higher redshifts and earlier times where the physical extent of the stellar component in galaxies is expected to be smaller, as there is less opportunity for them to have grown large stellar discs or haloes (McAlpine et al. 2019). This combination of vigorous, compact, and obscured star formation and an underdeveloped or absent extended unobscured stellar component suggests that the descendant system will be similarly compact, which has been previously been suggested would naturally link these descendants to the compact 'quiescent' and 'post-starburst' galaxies that exist at $z \sim 1$–2, and potentially higher redshifts (e.g. Simpson et al. 2014; Toft et al. 2014; Hodge et al. 2016; Almaini et al. 2017).

4 CONCLUSIONS

We use the large sample of ALMA-identified SMGs in the S2CLS UDS field from Stach et al. (2019), which are covered by ultradeep *K*-band imaging from UKIDSS UDS ($K = 25.3$, 5σ), to construct

a sample of $80\,K > 25.3$ mag SMGs with 870-μm detections of $\geq 4.8\sigma$ significance (equivalent to a false-positive rate of one source). We select a *K*-faint subset of 30 SMGs that are free of potential contamination of their multiband photometry by nearby galaxies and use these to infer the properties of the larger full $K > 25.3$ mag sample. In addition, we construct a *control* sample of 100 SMGs from the $K \leq 25.3$ mag population, matched in redshift and L_{IR}, to allow comparisons free of selection or evolutionary trends.

Based on our *K*-faint sample, we estimate that 15 ± 2 per cent of SMGs brighter than $S_{870} \geq 3.6$ mJy are fainter than $K = 25.3$ mag, rising to $\sim$25–30 per cent of those at $z \gtrsim 3$. We see no significant variation in this fraction with 870-μm flux density across $S_{870} = 3$–10 mJy. Hence, extrapolating to the lowest flux densities probed by AS2UDS, we estimate a surface density of $K > 25.3$ and $S_{870} \geq 1$ mJy SMGs of 450^{+750}_{-300} deg^{-2}. We caution that the latter estimate relies on the assumption that there is no strong variation in the proportion of *K*-faint SMGs between $S_{870} \sim 1$ and 3 mJy.

Using the MAGPHYS analysis of the AS2UDS SMGs presented in Dudzevičiūtė et al. (2020), we investigate the causes of the faintness of these SMGs in the near-infrared waveband and show that the redshift distribution of the *K*-faint SMG subset has a significantly higher median than the *K*-detected SMG subset: $z = 3.44 \pm 0.06$ versus $z = 2.36 \pm 0.11$.

We also show that the median *V*-band attenuation for the *K*-faint SMGs of $A_V = 5.2 \pm 0.3$, compared to $A_V = 2.9 \pm 0.1$ for our redshift-matched *control* sample, suggests that a combination of higher attenuation, as well as typically higher redshifts, is responsible for the faint near-infrared fluxes of the *K*-faint SMGs – as previously proposed by da Cunha et al. (2015), Dudzevičiūtė et al. (2020), and others.

Finally, we investigate the cause of the high dust attenuation in this subset of SMGs, compared to more average members of the population at the same redshifts. We find a trend of higher A_V for SMGs with smaller dust continuum sizes, suggesting that it is the compactness of the dust-obscured activity in these systems that is driving the high attenuations. We determine the relation of dust continuum sizes with far-infrared luminosity, finding a weak trend for more luminous sources to be more compact, and following on from this a relation between dust attenuation and far-infrared surface brightness, which shows a significant positive correlation. However, while the higher Σ_{IR}, and Σ_{SFR}, values of the K-faint SMGs indicate higher A_V values, we find that the K-faint SMGs still lie off this trend. We suggest that the behaviour of the $K > 25.3$ mag SMGs reflects details of the relative scales and mixture of dust obscuration and stellar populations in these systems; in particular, their properties suggest that any less obscured, spatially extended stellar component is generally absent in these galaxies. Testing this will require the deeper, high-resolution mid-infrared imaging that *James Webb Space Telescope* (*JWST*) can deliver.

We conclude that the K-faint SMGs represent the higher redshift, higher star formation rate density, and higher dust attenuation tail of the distribution of the wider SMG population. The existence of such systems cautions against using the presence or absence of a near-infrared counterpart as a test of the reality of a submillimetre source, as well as highlighting the potential incompleteness of any prior catalogues used to deblend far-infrared observations, if these lack complete interferometric submillimetre identifications. These galaxies also highlight the potential for incompleteness in purportedly 'mass'-selected surveys of galaxies at high redshifts, and the possibility of contamination in 'drop-out'-selected samples of very high redshift galaxies where the analysis fails to consider the possibility of foreground sources having very high dust attenuation, $A_V \gg 3$. The upcoming launch of the *JWST* holds significant promise for improving our understanding of the nature and properties of these examples of dust-obscured, star-forming galaxies at high redshifts – including measuring the size of any less obscured stellar components in the K-faint SMG population.

DATA AVAILABILITY

The data used in this paper can be obtained from the UKIRT, *Spitzer*, and ALMA data archives, as well as the UKIDSS UDS website (https://www.nottingham.ac.uk/astronomy/UDS).

REFERENCES

Algera H. et al., 2020, ApJ, 903, 138
Almaini O. et al., 2017, MNRAS, 472, 1401
An F.-X. et al., 2019, ApJ, 886, 48
Aravena M. et al., 2016, ApJ, 833, 68
Battisti A. J. et al., 2019, ApJ, 882, 61
Calistro Rivera G. et al., 2019, ApJ, 863, 56
Caputi K., Cirasulo M., Dunlop J. S., McLure R. J., Farrah D., Almaini O., 2011, MNRAS, 413, 162
Chen C. C. et al., 2015, ApJ, 799, 194
Coppin K. E. K., Halpern M., Scott D., Marsden G., Iwamuro F., Maihara T., Motohara K., Totani T., 2004, MNRAS, 354, 193
Cowie L. L., Barger A. J., Wang W.-H., Williams J. P., 2009, ApJ, 697, L122
Cowie L. L., Gonzalez-Lopez J., Barger A. J., Bauer F. E., Hsu L.-Y., Wang W.-H., 2018, ApJ, 865, 106
da Cunha E., Charlot S., Elbaz D., 2008, MNRAS, 388, 1595
da Cunha E. et al., 2015, ApJ, 806, 110
Dannerbauer H., Lehnert M. D., Lutz D., Tacconi L., Bertoldi F., Carilli C., Genzel R., Menten K. M., 2002, ApJ, 573, 473
Dannerbauer H., Lehnert M. D., Lutz D., Tacconi L., Bertoldi F., Carilli C., Genzel R., Menten K. M. 2004, ApJ, 606, 664
Dannerbauer H., Walter F., Morrison G., 2008, ApJ, 673, L127
Dey A., Graham J. R., Ivison R. J., Smail I., Wright G. S., Liu M. C., 1999, ApJ, 519, 610
Dudzevičiūtė U. et al., 2020, MNRAS, 494, 3828
Dunlop J. S. et al., 2004, MNRAS, 350, 769
Dunlop J. S. et al., 2017, MNRAS, 466, 861
Everett W. B. et al., 2020, ApJ, 900, 55
Franco M. et al., 2018, A&A, 620, 152
Frayer D. T., Reddy N. A., Armus L., Blain A. W., Scoville N. Z., Smail I., 2004, AJ, 127, 728
Garn T., Best P. N., 2010, MNRAS, 409, 421
Geach J. E. et al., 2017, MNRAS, 465, 1789
Gullberg B. et al., 2019, MNRAS, 490, 4956
Harwit M., Houck J. R., Soifer B. T., Palumbo G. G. C., 1987, ApJ, 315, 28
Hodge J. A. et al., 2013, ApJ, 768, 91
Hodge J. A. et al., 2016, ApJ, 833, 103
Hodge J. A. et al., 2019, ApJ, 876, 130
Houck J. R., Schneider D. P., Danielson G. E., Beichman C. A., Lonsdale C. J., Neugebauer G., Soifer B. T., 1985, ApJ, 290, L5
Ikarashi S. et al., 2011, MNRAS, 415, 3081
Ikarashi S. et al., 2015, ApJ, 810, 133
Ikarashi S. et al., 2017, ApJ, 835, 286
Im M., Yamada T., Tanaka I., Kajisawa M., 2002, ApJ, 578, L19
Ivison R. J., Smail I., Barger A. J., Kneib J.-P., Blain A. W., Owen F. N., Kerr T. H., Cowie L. L., 2000, MNRAS, 315, 209
Ivison R. J. et al., 2007, MNRAS, 380, 199
Karim A. et al., 2013, MNRAS, 432, 2
Lagos C. d. P. et al., 2020, MNRAS, 499, 1948
Lawrence A. et al., 2007, MNRAS, 379, 1599
McAlpine S. et al., 2019, MNRAS, 488, 2440
Mobasher B. et al., 2005, ApJ, 635, 832
Negrello M. et al., 2010, Science, 330, 800
Pirzkal N., Rothberg B., Ryan R., Coe D., Malhotra S., Rhoads J., Noeske K., 2013, ApJ, 775, 11

Pope A., Borys C., Scott D., Conselice C., Dickinson M., Mobasher B., 2005, MNRAS, 358, 149

Reshef D. et al., 2011, Science, 334, 6062

Rowan-Robinson M. et al., 1991, Nature, 351, 719

Schreiber C. et al., 2018, A&A, 618, 85

Scoville N. Z., 2013, in Falcon-Barroso J., Knapen J. H., eds, Secular Evolution of Galaxies. Cambridge Univ. Press, Cambridge, p. 491

Simpson C. J., Westoby P., Arumigam V., Ivison R. J., Hartley W., Almaini O., 2013, MNRAS, 433, 2647

Simpson J. M. et al., 2014, ApJ, 788, 125

Simpson J. M. et al., 2017, ApJ, 844, L10

Simpson J. M. et al., 2020, MNRAS, 495, 3409

Smail I., Ivison R. J., Kneib J.-P., Cowie L. L., Blain A. W., Barger A. J., Owen F. N., Morrison G., 1999, MNRAS, 308, 1061

Stach S. M. et al., 2018, ApJ, 860, 161

Stach S. M. et al., 2019, MNRAS, 487, 4648

Swinbank A. M. et al., 2012, MNRAS, 427, 1066

Swinbank A. M. et al., 2014, MNRAS, 438, 1267

Tadaki K.-I. et al., 2020, ApJ, 901, 74

Toft S. et al., 2014, ApJ, 782, 68

Umehata H. et al., 2020, A&A, 640, L8

van der Wel A. et al., 2014, ApJ, 788, 28

Walter F. et al., 2012, Nature, 486, 233

Wang W.-H., Cowie L. L., van Saders J., Barger A. J., Williams J. P., 2007, ApJ, 670, L89

Wang W.-H., Cowie L. L., Barger A. J., Williams J. P., 2011, ApJ, 726, L18

Wang T. et al., 2019, Nature, 572, 211

Weiss A., Ivison R. J., Downes D., Walter F., Cirasuolo M., Menten K. M., 2009, ApJ, 705, L45

Williams C. C. et al., 2019, ApJ, 884, 154

Yamaguchi Y. et al., 2019, ApJ, 878, 73

Zhou L. et al., 2020, A&A, 642, 155

This paper has been typeset from a TEX/LATEX file prepared by the author.